Computed and Experimental Surface Pressure and Heating on 70-Deg Sphere Cones

K. James Weilmuenster* and H. Harris Hamilton II†
NASA Langley Research Center, Hampton, Virginia

A comparison of computed and experimental surface pressure and heating on 70-deg sphere cones at angles of attack up to 20 deg is presented. The sphere cone geometries were varied by changing the bluntness ratio and corner radius of the configuration. A three-dimensional Euler flowfield solution yielded surface pressures and was coupled with an axisymmetric analogue technique to determine surface heating. These computational results have then been compared with available experimental data.

Nomenclature

C_A = axial force coefficient
C_M = longitudinal pitching moment coefficient
C_N = normal force coefficient
C_P = pressure coefficient
D = drag, N
L = reference axial length, m, or lift, N
M = Mach number
P = pressure, N/m^2
q = surface heating rate, MW/m^2
R = spherical coordinate
R_e = unit Reynolds number, 1/m
S = surface length, m
U = total velocity, m/s
x = Cartesian coordinate
y = Cartesian coordinate
z = Cartesian coordinate
α = angle of attack, deg
γ = ratio of specific heats
ϕ = spherical coordinate
ρ = density, Kg/m^3
θ = spherical coordinate

Subscripts

b = base
c = corner
N = nose
ref = reference condition
w = wall
∞ = freestream condition

Introduction

THE success of the space shuttle has opened the door for many near and far technological opportunities. To support some of these activities, a new family of space vehicles, known as aeroassist orbital transfer vehicles (AOTV), has been proposed. A review of several aeroassist vehicle concepts is given by Walberg in Ref. 1. These vehicles typically operate in the upper reaches of the atmosphere at higher velocities and lower pressures than so-called re-entry vehicles and utilize their aerodynamic characteristics to either maneuver in the upper atmosphere or to lose enough ΔV, in either single or multiple passes, to drop into a lower energy orbit.

Many forebody shapes have been proposed for these vehicles. For the most part, they are very blunt, nonaxisymmetric bodies whose shapes are designed to maximize the aerodynamics while minimizing the effects of heating. The analysis and prediction of the flight characteristics of such vehicles in an entry environment are certainly not a new technology. Almost all entry shapes used for scientific purposes are very blunt, i.e., the heat shields on the Mercury, Gemini, and Apollo capsules and atmospheric probes such as Viking and Galileo. These types of vehicles were designed based on tests in ground-based facilities and on information obtained from computer codes that were limited to two-dimensional or axisymmetric analysis of the flowfield.

The design of aeroassist vehicles will once again require detailed testing in ground-based facilities. But, methods for numerical flowfield analysis will have to be much more sophisticated than those used in the past for two reasons. First, these vehicles will depend on their aerodynamics for maneuverability, and to determine aerodynamics, the entire three-dimensional flowfield will have to be generated. Second, the operational environment, high velocity, and low pressure will introduce the effects of chemistry (both equilibrium and nonequilibrium) and radiation in the flowfield that will have a significant impact on vehicle heating as well as on the aerodynamics.

In previous papers,[3-6,8] we have demonstrated an ability to predict flowfields about, and surface heating on, complex three-dimensional bodies in the supersonic/hypersonic flow regimes. In this paper, we will outline how this methodology may be used to address some of the computational problems outlined here and present some current results.

When picking an initial configuration to work with, we wanted a simple geometrical shape so that geometry description and computational problems could be uncoupled, a configuration that had an adequate data base and a shape that

Presented as Paper 86-0567 at the AIAA 24th Aerospace Sciences Meeting, Reno, NV, Jan. 6-9, 1986; received Oct. 6, 1986; revision received March 11, 1987.

*Aerospace Technologist, Aerothermodynamics Branch, Space Systems Division. Member AIAA.

†Research Leader, Aerothermodynamics Branch, Space Systems Division. Member AIAA.

might qualify as an AOTV configuration. Previous studies[2] have shown that a vehicle with an L/D in the range of at least 0.2 to 0.4 is required to effectively carry out an AOTV mission. A 70-deg sphere cone with a bluntness ratio of 0.5 and a sharp corner—the Viking aeroshell shape—fits all three of these requirements and was selected as the baseline configuration for the work presented in this paper.

Geometries

The bodies used in this study will consist of two 70 deg sphere cones with ratios of nose radius to base radius, R_N/R_b, of 1.0 and 0.5. For each R_N/R_b, there will be three corner configurations, a sharp corner and corners with ratios of corner radius to base radius, R_c/R_b, of 0.0625 and 0.125. Figures 1a and 1b show frontal and side views of a typical body as described by the computational mesh that, for clarity, has had every other grid line deleted. The body is described in a spherical coordinate system as noted in Figs. 1a and 1b along with the corresponding Cartesian coordinates. Each body is fitted with a "skirt" that serves two purposes. The first is to move the outflow boundary well downstream of the forebody to eliminate the possibility of this boundary affecting flow on the forebody and second, in the case of the sharp-cornered body, to drive the surface Mach number supersonic at the corner. For the bodies with a corner radius, the skirt lies parallel to the body centerline. Figure 1c shows a perspective view of the body. Since the body is symmetric about the symmetry plane, only one half of the flowfield is actually computed.

Computational Techniques

Flowfield Computations

The HALIS inviscid flowfield code was initially developed to handle the high angle-of-attack flowfields about the shuttle vehicle, which were characterized by large regions of embedded subsonic flow on the windward surface. Since, depending on each particular design, all or a large portion of the aeroassist vehicle's surface, as well as its outer flowfield flow, will be subsonic, we felt that the same methodology used for the shuttle could be used for the aeroassist vehicles.

The HALIS code is described in great detail in Ref. 5. Briefly, the code is a time-asymptotic solution of the Euler equations that utilizes an unsplit MacCormack differencing scheme. The solution space is the volume between the body surface and the bow-shock wave, which is treated as a time-dependent boundary. This leads to a coordinate system defined by the position of the bow shock and the body, as well as the spatial derivatives along these surfaces. The HALIS code uses a spherical coordinate system to describe the nosecap region of a vehicle and is matched to a cylindrical coordinate system that describes the rest of the vehicle. For the present computations, it was felt that the body would be best described in the spherical system alone. Thus, a spherical-system-only version of HALIS has been created for this work. In addition, two additional coordinate transformations have been added to the code. The first compresses the grid at the wall for greater radial resolution, and the second is used to distribute grid points in the θ direction for greater resolution of the flow at the body-skirt juncture as can be seen in Fig. 1.

The code is written in vector Fortran for the CDC VPS-32 and uses 64-bit words. Run times vary with configuration and angle of attack, but average 15 minutes of CPU time for a flowfield containing 27,000 points.

Surface Heating

The surface heating rates are calculated using the axisymmetric analogue for three-dimensional boundary layers developed by Cooke.[7] The details of the present method are described in Ref. 8. Briefly, the general three-dimensional boundary-layer equations written along streamlines reduce to the axisymmetric form when the crossflow in the boundary layer is neglected. The distance along a streamline is interpreted as distance along an equivalent axisymmetric body, and the metric associated with the spreading of the streamlines is interpreted as the radius of the equivalent axisymmetric body. This allows any axisymmetric boundary-layer solution to be used to calculate the approximate three-dimensional heating rates along streamlines, which greatly simplifies the problem. By considering multiple streamline paths, the heating over a complete vehicle can be computed at a fraction of the cost that would be required if the full three-dimensional boundary-layer equations were used.

In the present approach, a noniterative, single-pass technique, the inviscid solution from HALIS is used to compute the streamline information. To calculate the boundary-layer solution along these streamlines, an approximate integral method,[9] with corrections[10] added to account for the large velocity gradients that occur in the present application, has been used. The results presented in this paper are limited to laminar flow. Also, the effect of entropy swallowing has not been included in the calculations. However, since the configuration in question is very blunt and the solutions are being compared with wind-tunnel data, the effect of entropy swallowing on the results should be very small. Since the effects of entropy swallowing are being neglected, the boundary-layer edge properties are taken to be the surface values in the inviscid solution.

Results

The flowfields for all of the bodies mentioned in the geometries section have been computed for $M_\infty = 10$ and $\gamma = 1.4$ at angles of attack of 0, 5, 10, 15, and 20 deg. The computational results presented in this paper have been limited to the $R_N/R_b = 0.5$ body, since experimental pressure and heating data are currently available for this shape with the $R_c/R_b = 0$ configuration and it was found that the bluntness ratio had little effect on the computational results. For this particular shape, the same used for the Viking aeroshell, there is a large surface pressure database documented in Ref. 11. In Fig. 2, the comparison of experimental and computed surface pressure coefficients, C_P, in the symmetry plane is quite good for this zero angle-of-attack case in which the experimental data were taken with the body at $\alpha = 0.3$ deg. The windward surface corresponds to positive S/R_b and the lee surface to negative S/R_b. For this and succeeding plots, quantities on the skirt of the body have not been plotted. The same symmetry plane plot for an $\alpha = 20$ deg is shown in Fig. 3. Again, the agreement between experimental and computed C_P is quite good. The breaks in the computed C_P curves at a $S/R_b \approx \pm 0.2$ are due to the surface curvature discontinuity at the juncture of the sphere and cone and are evident in the leeside experimental data. Figure 4 gives comparisons of computed and experimental C_P in the planes $\phi = 0$, 30, and 60 deg. The most notable point here is that the effect of the sphere/cone juncture on the pressure distribution becomes quite pronounced when moving from the windward to leeward surface. A more comprehensive picture of the surface pressure distribution can be seen in Fig. 5, which is a surface contour plot of $P_w/\rho_\infty U_\infty^2$ for the $\alpha = 20$ deg case, where the viewing angle is coincident with the body axis. The sphere/cone juncture can be traced by following the contour line discontinuities around the center of the body, and the stagnation point lies roughly halfway between the center and the outer rim of the body.

Figure 6 indicates the effect of corner radius on surface pressure. Here, in Fig. 6a, the pressure coefficient in the symmetry plane is plotted as a function of positive z/L for the windward surface and negative z/L for the lee surface where the pressures have been plotted to the point of tangency with the aft skirt. The effect of corner radius on the pressure field is confined to the outer edge of the body where the effect is quite pronounced. Similar effects are seen in the off-axis pressure plots at

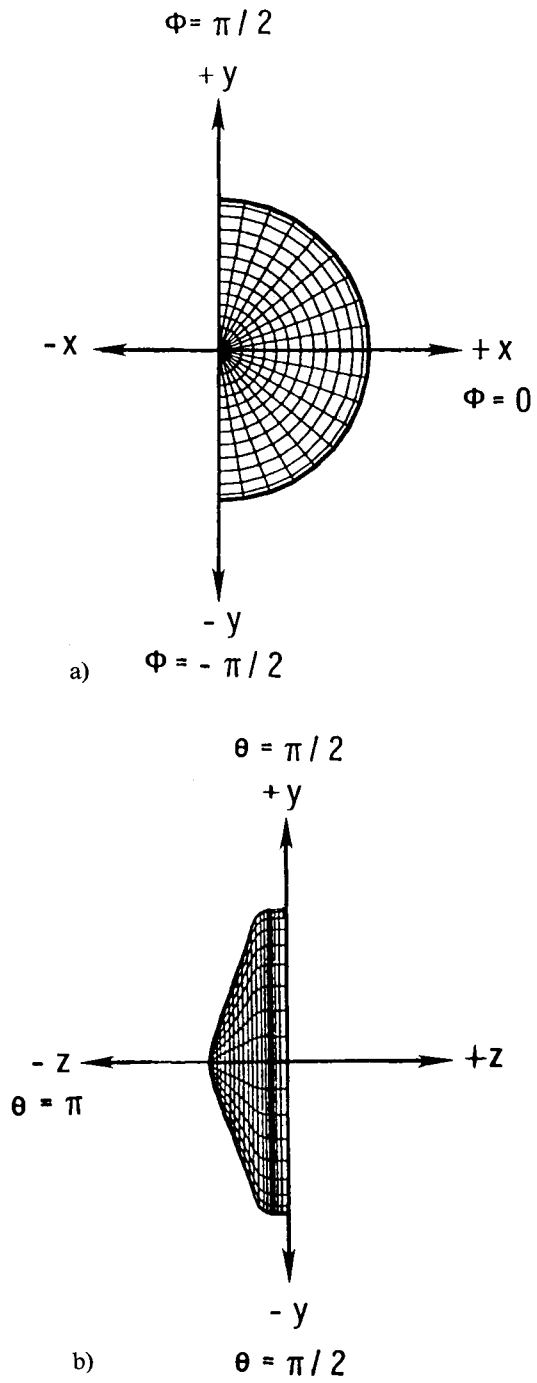

Fig. 1 Body geometry and associated coordinate systems. a) Frontal view. b) Side view. c) Perspective.

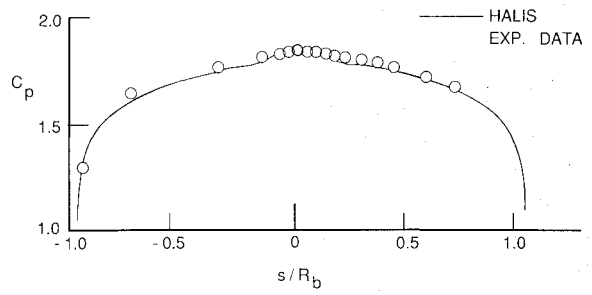

Fig. 2 Symmetry plane pressure coefficient distribution at $M_\infty = 10.0$, $\gamma = 1.4$, and $\alpha = 0$ deg.

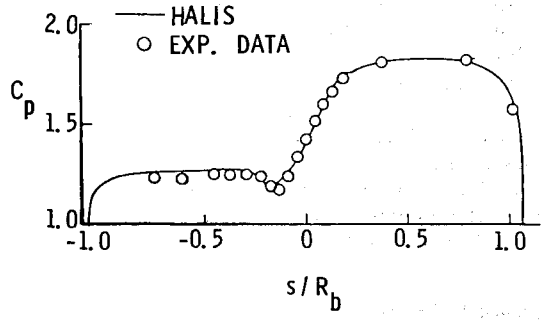

Fig. 3 Symmetry plane pressure coefficient distributions at $M_\infty = 10.0$, $\gamma = 1.4$, and $\alpha = 20$ deg.

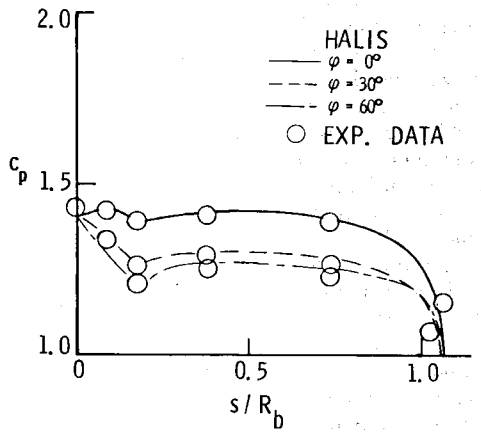

Fig. 4 Off-symmetry plane pressure coefficient distribution at $M_\infty = 10.0$, $\gamma = 1.4$, and $\alpha = 20$ deg.

$\phi = -45$ deg, Fig. 6b, $\phi = 0.0$ deg, Fig. 6c, and $\phi = 45$ deg, Fig. 6d.

The integrated effect of corner radius can be seen by comparing the aerodynamic characteristics of the bodies. The effect of corner radius on drag is indicated in Fig. 7, where a larger corner radius results in less drag for all angles of attack. This reduction in drag with increasing corner radius is a direct result of coupling the lower surface pressures due to the expansion with the large percentage of total wetted surface area that is present near the outer edges of the configuration. The effects of base drag have not been included in these computations. However, as seen in Fig. 7b, the larger corner radius also produces less lift and negative C_L values, a characteristic of very blunt bodies, which is due to the large difference in magnitude between C_A and C_N. L/D values, as seen in Fig. 7c, are not greatly

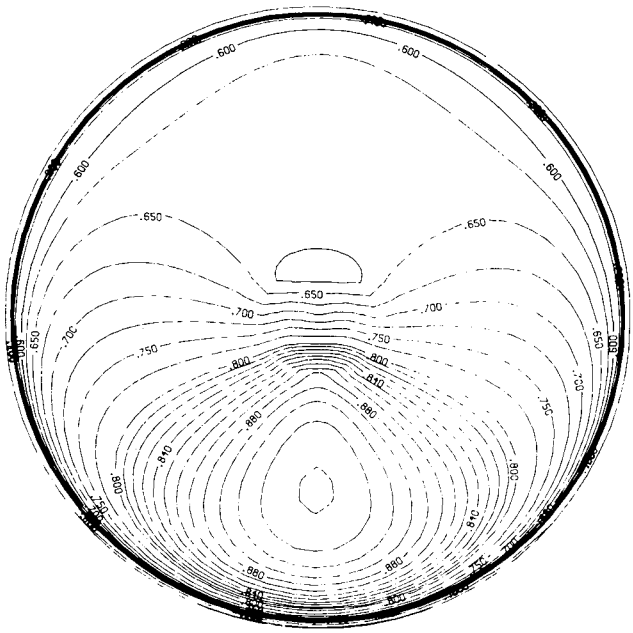

Fig. 5 Surface contour plot of $P_w/\rho_\infty U_\infty^2$ at $M_\infty = 10.0$, $\gamma = 1.4$, and $\alpha = 20$ deg.

affected by corner radius. A similar trend can be seen in the pitching moment results, Fig. 7d, where the effect of corner radius on C_M is relatively small. The aerodynamic results presented here are for both bluntness ratio bodies, since we found that the bluntness ratio had virtually no effect on the computed aerodynamics.

As previously mentioned, one of the reasons for the current approach to the problem is that it can handle the large regions of subsonic flow embedded in the flowfield. The extent of the subsonic flow can be seen for the $R_b/R_N = 0.5$, $R_c/R_b = 0$ body at $\alpha = 20$ deg by referring to Fig. 8. Here, the Mach number has been contoured between the shock and body in the symmetry plane, and the subsonic region has been shaded. Obviously, the subsonic regime is very large and wets the entire surface of the body. Note that the skirt accomplishes its purpose of driving the flow supersonic at the corner and providing a supersonic outflow boundary.

The axisymmetric analog heating analysis is implemented by integrating along body surface streamlines. Figure 9 shows those surface streamlines on $R_N/R_b = 0.5$, $R_c/R_b = 0.125$ body at angles of attack of 0, 10, and 20 deg over half of the body surface. The surface streamlines are plotted on half-tone photographs of surface pressure color contour plots where the body has been rotated slightly to produce a perspective view. The half-tones do not offer a lot of information except that there is little variation of pressure over the body surface, except as indicated by the dark rim around the body that reflects the

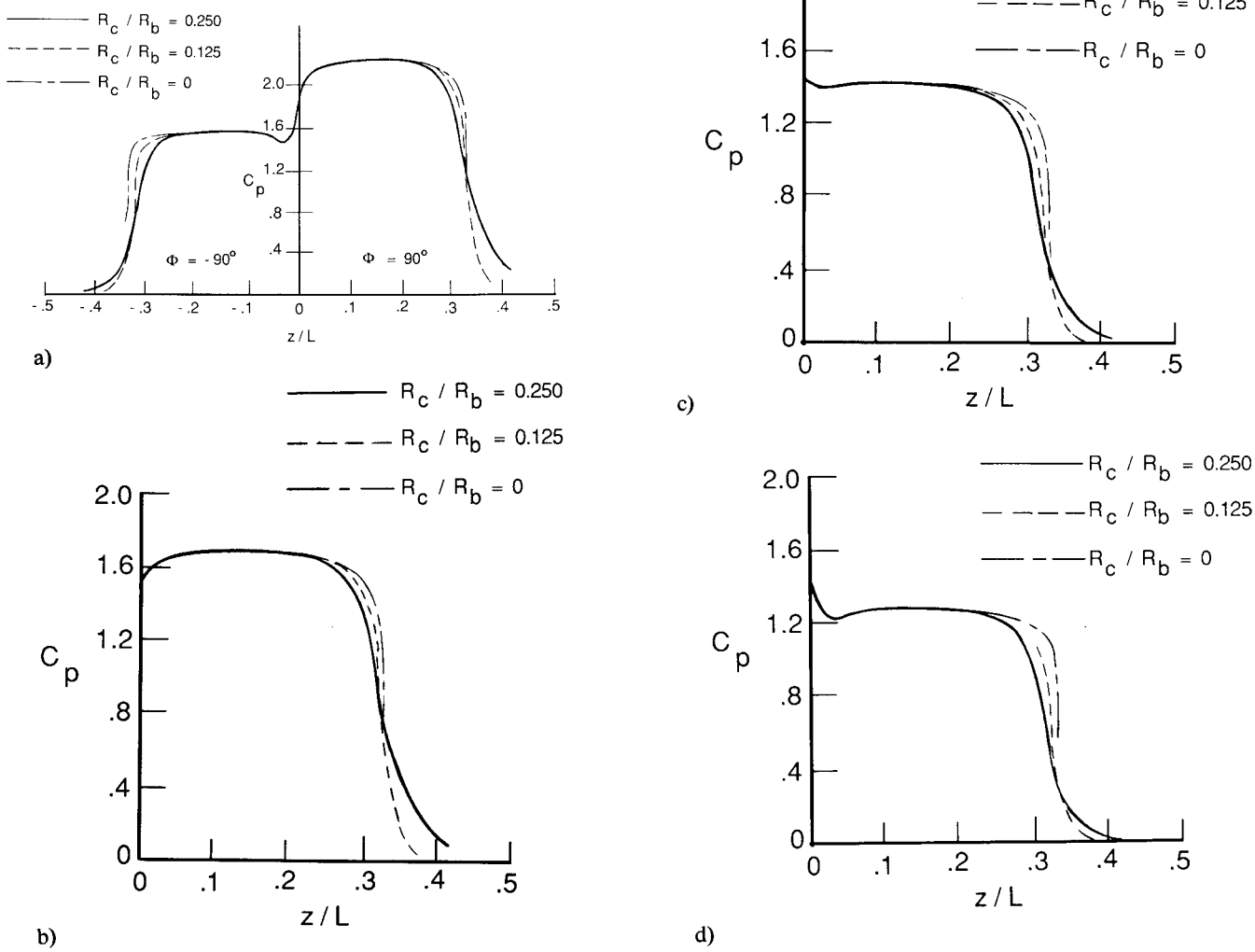

Fig. 6 Surface pressure plots, $M_\infty = 10.0$, $\gamma = 1.4$, and $\alpha = 20$ deg. a) Symmetry plane $\phi = -90$ deg and $\phi = 90$ deg. b) $\phi = -45$ deg. c) $\phi = 0.0$ deg. d) $\phi = 45$ deg.

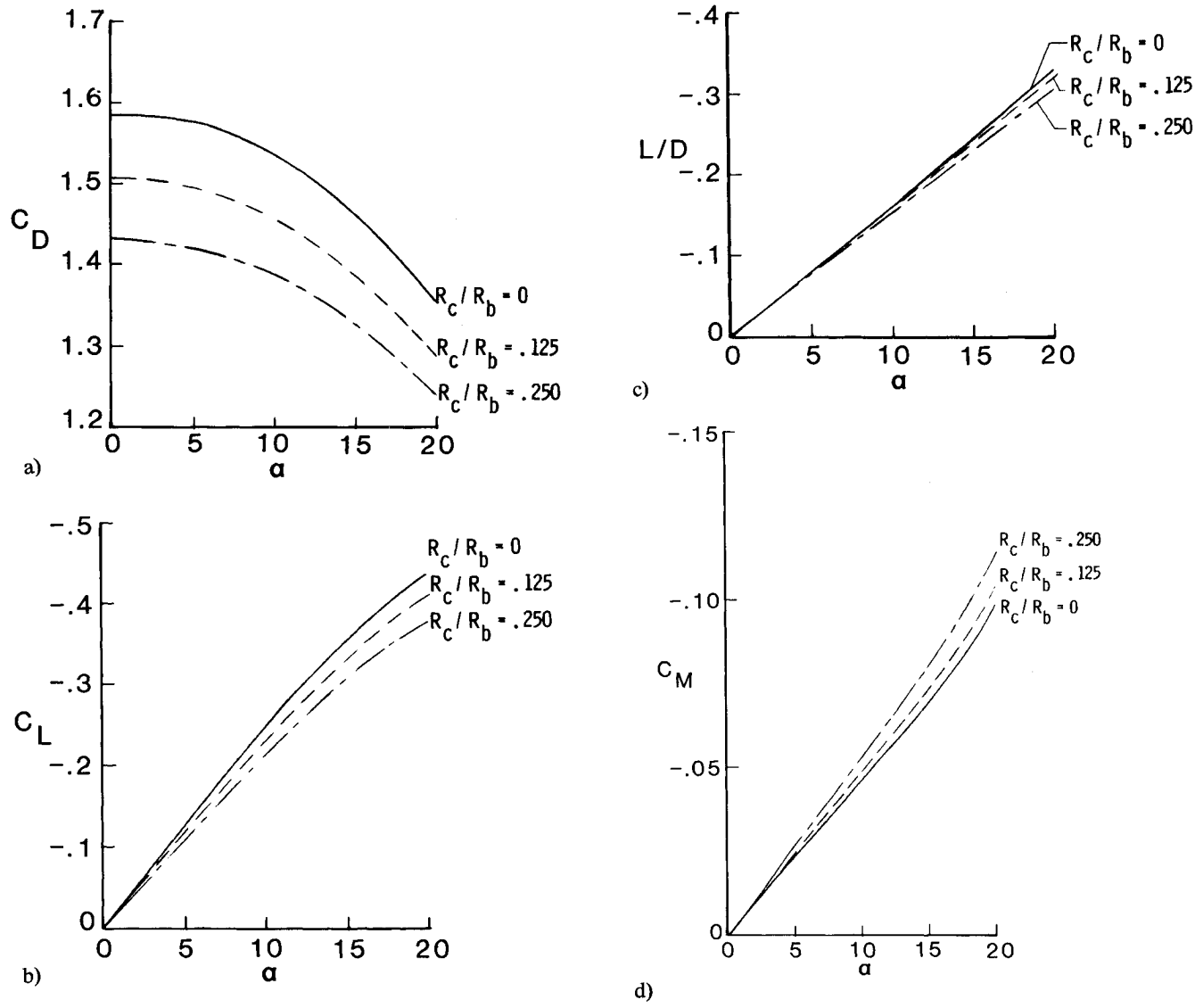

Fig. 7 Aerodynamic characteristics of 70 deg sphere cone at $M_\infty = 10.0$, and $\gamma = 1.4$. a) Drag coefficient. b) Lift coefficient. c) Lift/drag ratio. d) Pitching moment coefficient.

pressure relief offered by the corner radius. Unlike flow over small half-angle cones where the streamlines quickly wrap around to the leeside of the body because of the low surface pressure there, the relatively high leeside pressures found on these bodies force the streamlines to move away from the stagnation point in a radial pattern. As can be seen by comparing Figs. 9b and 9c, as the angle of attack increases, the leeside streamline pattern is significantly changed by the presence of the spherical nose cap. In Fig. 10 is shown the effect of corner radius on the streamline pattern of the $R_N/R_b = 0.5$ body at $\alpha = 20$ deg. The $R_c/R_b = 0.0$ plot, Fig. 10a, shows no pressure relief at the corner and has the highest leeside pressure of the cases shown previously in Fig. 10 and as indicated in the halftones. A comparison of Figs. 10a and 10c indicates that the pressure relief afforded by the corner radius has a significant impact on the surface streamline pattern.

Heating

In the present paper, calculated heating rates on a spherically blunted 70 deg half-angle cone with $R_N/R_b = 0.5$ are presented. Results for $R_c/R_b = 0$, 0.0625, and 0.125 are considered to investigate the effect of corner radius on surface heating. For all cases, the Mach number is 9.86 and the freestream unit Reynolds number is 1.8×10^6 per meter. For the sharp corner case ($R_c/R_b = 0$), the calculated results are compared with unpublished, experimental data obtained in the 31-in. Mach 10 tunnel at the Langley Research Center by C. Miller and R. Midden.

The results for the sharp corner body at $\alpha = 0$ deg are shown in Fig. 11. The nature of the heating for this case is different than that for lower half-angle cones with which the reader is probably more familiar. The heating over the forward portion of the cone decreases downstream of the stagnation point. However, aft of $z/L = 0.6$, the heating increases rapidly and approaches the stagnation value near the corner ($z/L = 1.0$). This rise in heating near the corner is caused by the rapid acceleration of the flow in this region as can be seen from the pressure distributions in Fig. 2.

The results for the sharp corner body at $\alpha = 20$ deg are shown in Fig. 12. Comparisons are shown for both the most windward symmetry plane where $\phi = -90$ deg and the most leeward symmetry plane where $\phi = 90$ deg. For this case, the angle of attack is so large that the stagnation point has moved off the sphere and is located along the most windward ray ($\phi = -90$ deg) of the cone at $z/L = 0.53$; thus, the flow is much more complex than for the $\alpha = 0$ deg case shown in the previous figure. If we look first at the data, the heating is reasonably constant along the most windward symmetry plane of the cone in the stagnation region, but it increases near the

nose ($z/L = 0$) and the corner ($z/L = 1.0$). These increases are both due to the rapid acceleration of the flow and to the increased three-dimensional effects in these regions. As the flow expands around the nose and moves on to the most leeward symmetry plane ($\phi = 90$ deg), the heating decreases until the corner is approached, where it again increases.

There are oscillations in the heating solution near the stagnation point at $\alpha = 20$ deg (Fig. 12) that did not occur at $\alpha = 0$ deg (Fig. 11). As noted previously, the flowfield structure over the cone is much more complex at the higher angle of attack, and the resolution of the solution around the stagnation point is much lower. This leads to a less accurate definition of the boundary-layer edge conditions around the stagnation point at the higher angle of attack that is thought to produce the wiggles. However, the effect appears to be localized since the oscillations dissipate rapidly as the distance from the stagnation point increases.

Calculated results are shown in Fig. 13 at $\alpha = 20$ deg angle of attack for the three different corner radii ($R_c/R_b = 0$, 0.0625, and 0.125). The calculated results shown in Fig. 13a for $R_c/R_b = 0$ are the same as those shown previously in Fig. 12 but without the experimental data. The calculated results for $R_c/R_b = 0.0625$ and 0.125 are shown in Figs. 13b and 13c respectively. No experimental data exist at the present time for these two larger corner radii.

As might be expected, increasing the corner radius moves the stagnation point forward, from $z/L = 0.53$ in Fig. 13a to $z/L = 0.39$ in Fig. 13c. However, there is relatively small effect on the heating on the cone except near the juncture of the cone and afterbody. In general, the peak in heating on the aft end of the cone moves upstream and decreases as the corner radius is increased. Thus, adding an afterbody with a generous radius to the conical forebody is shown to be effective in reducing the magnitude of heating rate near the end of the body.

Circumferential distributions of calculated heating rate are presented in Fig. 14 for the sharp cornered body ($R_c/R_b = 0$) at

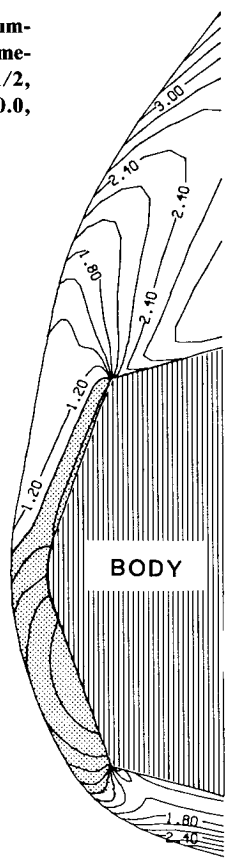

Fig. 8 Flowfield Mach number contour plot in the symmetry plane of a $R_N/R_b = 1/2$, $R_c/R_b = 0.0$ body at $M_\infty = 10.0$, $\gamma = 1.4$, and $\alpha = 20$ deg.

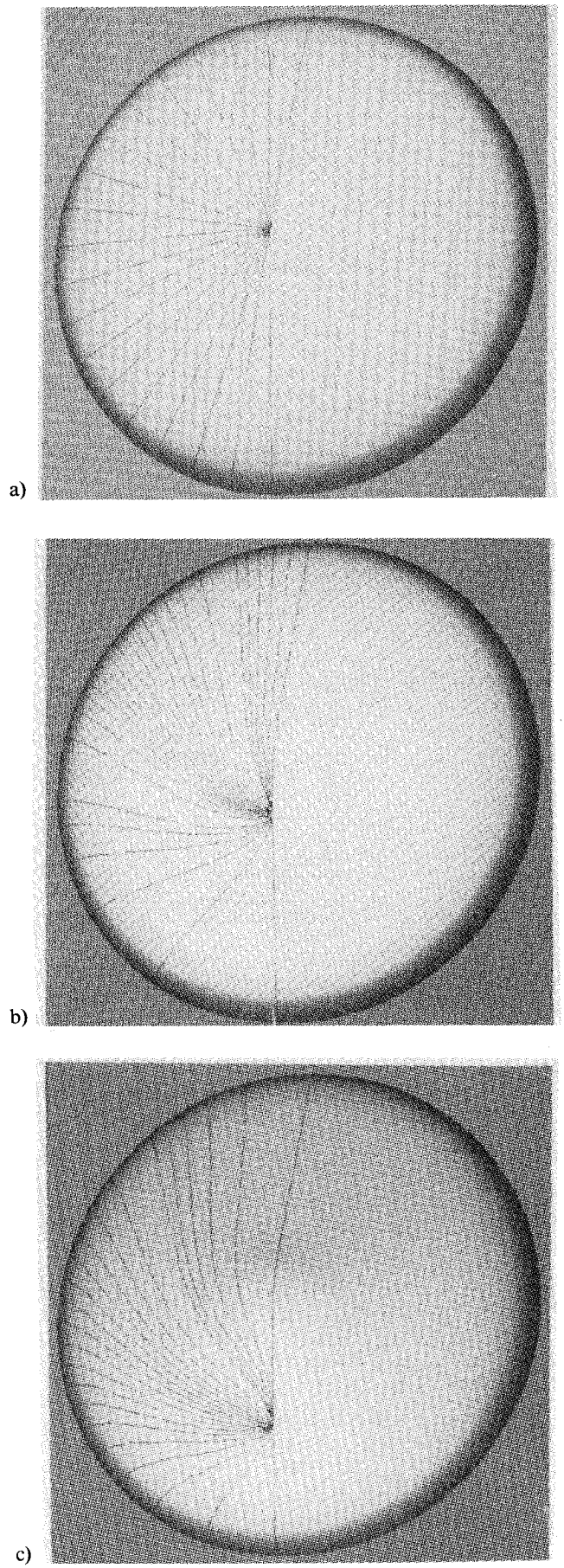

Fig. 9 Surface streamlines, 70 deg sphere cone, $M_\infty = 10.0$, $\gamma = 1.4$, $R_N/R_b = 0.5$, and $R_c/R_b = 0.125$. a) $\alpha = 0$ deg. b) $\alpha = 10$ deg. c) $\alpha = 20$ deg.

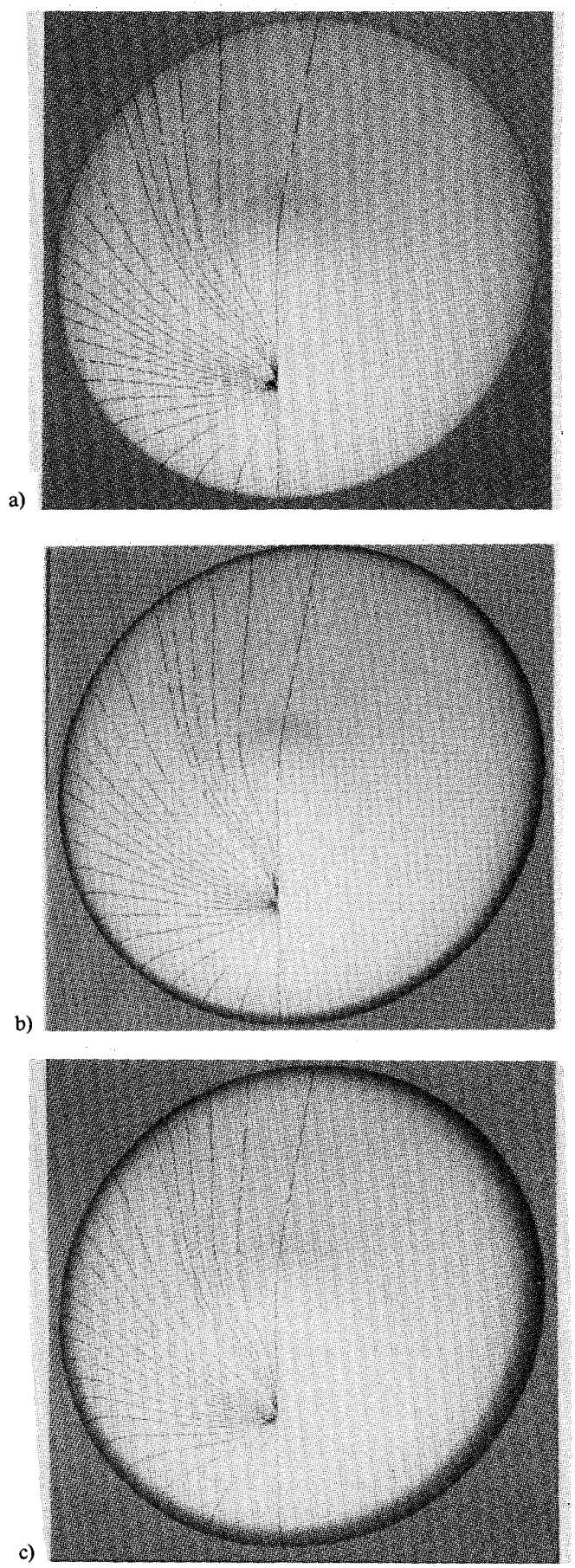

Fig. 10 Surface streamlines, 70 deg sphere cone, $M_\infty = 10.0$, $\gamma = 1.4$, $R_N/R_b = 0.5$, and $\alpha = 20$ deg. a) $R_c/R_b = 0$. b) $R_c/R_b = 0.0625$. c) $R_c/R_b = 0.125$.

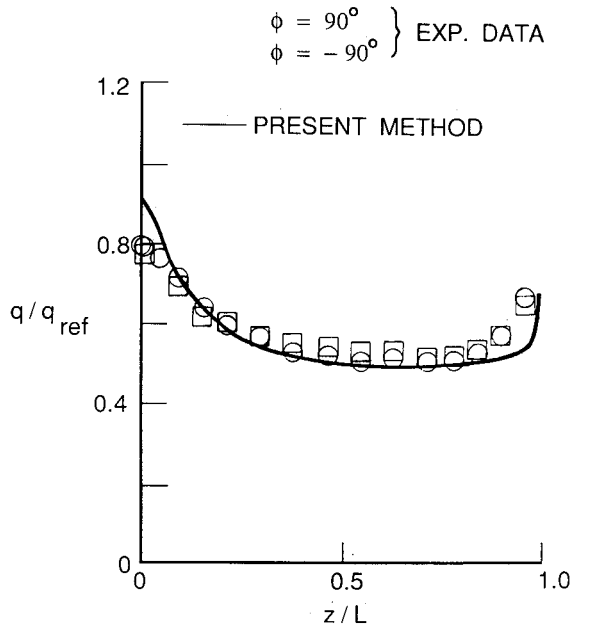

Fig. 11 Surface heating on spherically blunted, 70 deg cone, $M_\infty = 9.86$, $\gamma = 1.4$, $R_e = 1.8 \times 10^6$/m, and $\alpha = 0$ deg.

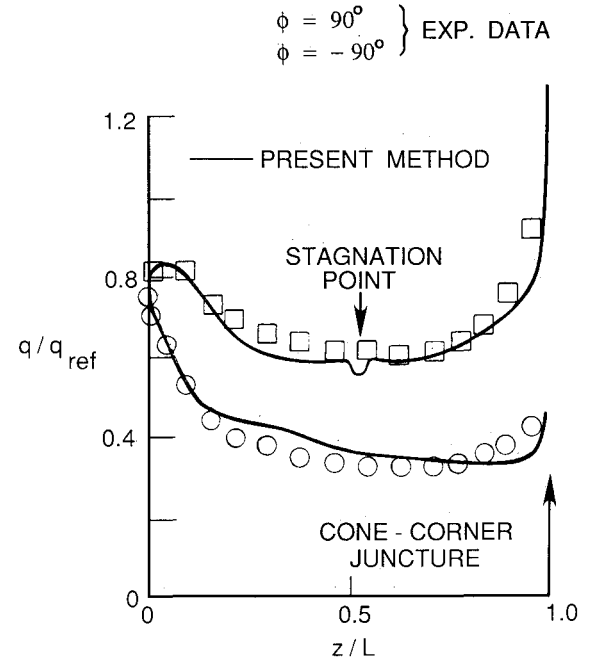

Fig. 12 Surface heating on spherically blunted, 70 deg cone, $M_\infty = 9.86$, $\gamma = 1.4$, $R_e = 1.8 \times 10^6$/m, and $\alpha = 20$ deg.

$\alpha = 20$ deg. Results are shown at three axial locations: $z/L = 0.3$, 0.6, and 0.9. There are no experimental data available for these conditions. The most interesting point to note is that the difference in heating rate on the most windward and most leeward rays of the cone is much smaller than might be expected based on experience with lower half-angle cones.[12] For the present 70 deg half-angle cone at $\alpha = 20$ deg, the most leeward ray on the cone is not shadowed and the heating near this ray is still relatively high.

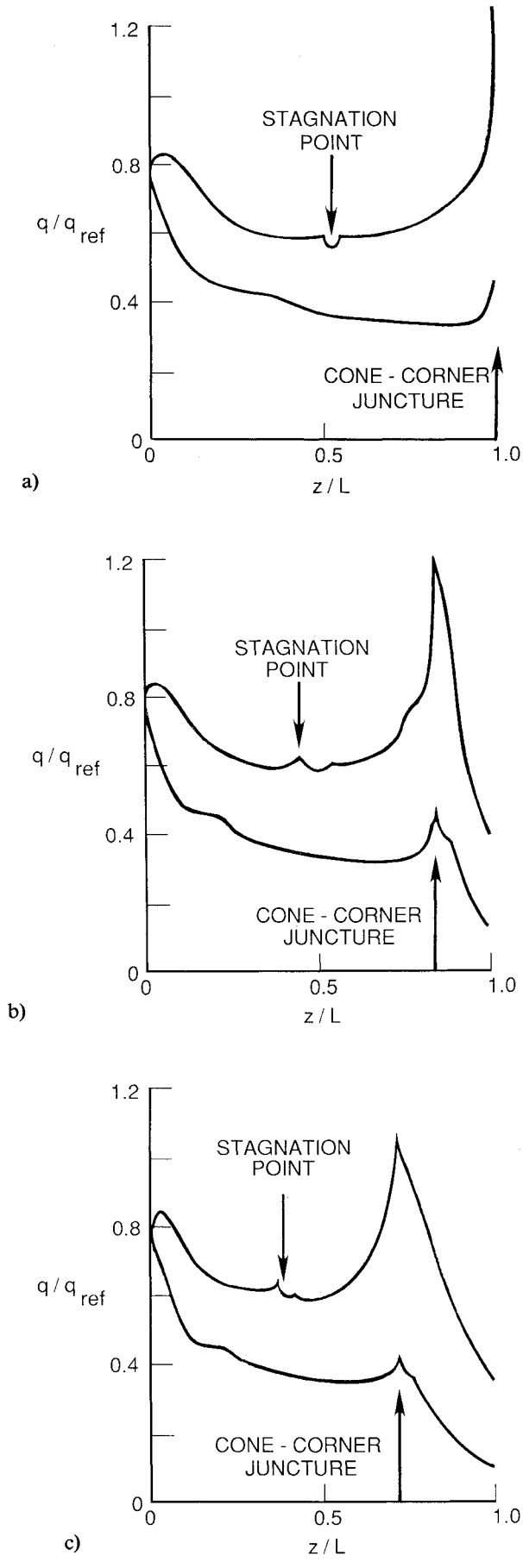

Fig. 13 Surface heating vs. axial length, $M_\infty = 9.86$, $\gamma = 1.4$, $R_{e_N} = 1.8 \times 10^6$/m, $R_N/R_b = 1/2$, and $\alpha = 20$ deg. a) $R_c/R_b = 0.0$. b) $R_c/R_b = 0.0625$. c) $R_c/R_b = 0.125$.

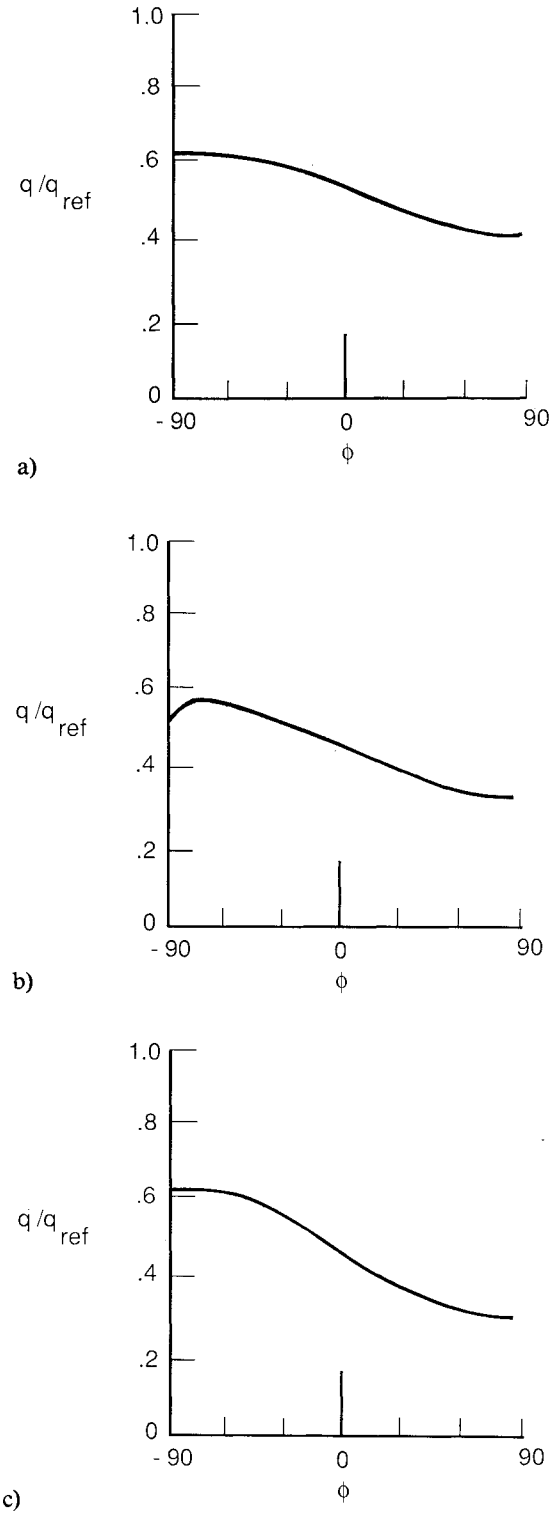

Fig. 14 Meridional surface heating distributions, $M_\infty = 10.0$, $\gamma = 1.4$, $R_{e_N} = 1.8 \times 10^6$/m, $R_N/R_b = 1/2$, and $R_c/R_b = 0.0$. a) $z/L = 0.3$. b) $z/L = 0.6$. c) $z/L = 0.9$.

Concluding Remarks

A method for handling the flowfields about 70 deg sphere cones at angles of attack up to 20 deg has been described. Surface pressure and heating results have been compared with existing wind-tunnel data. Computed surface pressures have been shown to be in excellent agreement with the experimental data, whereas the surface heating from approximate forms of the boundary-layer equations are in good agreement with the

experimental data. Analysis of the computed data showed that the effect of the bluntness ratio on surface pressures and heating was very small. However, body corner radius, while not having a significant impact on body aerodynamics, produced large changes in surface pressure and heating distribution.

The results indicate that the solution techniques outlined in this paper generate good results for a simple geometrical shape. Next, these techniques will be applied to more complex configurations such as the AFE flight experiment vehicle. Also, real-gas chemistry will be added to the codes so that actual AFE flight conditions can be simulated.

References

[1]Walberg, G. D., "A Survey of Aeroassisted Orbit Transfer," *Journal of Spacecraft and Rockets*, Vol. 22, Jan./Feb. 1985, pp. 3–18.

[2]Talay, T. A., White, N. W., and Naftel, J. C., "Impact of Atmospheric Uncertainties and Viscous Interaction Effects on the Performance of Aeroassisted Orbital Transfer Vehicles," Thermal Design of Aeroassisted Orbital Transfer Vehicles; *Progress in Astronautics and Aeronautics*, Vol. 96, edited by H. F. Nelson, AIAA, New York, 1985, pp. 198–229.

[3]Weilmuenster, K. J. and Hamilton, H. H. II, "A Method for Computation of Inviscid Three-Dimensional Flow over Blunt Bodies Having Large Embedded Subsonic Regions," AIAA Paper 81-1203, June 1981.

[4]Weilmuenster, K. J. and Hamilton, H. H. II, "A Comparison of Computed Space Shuttle Orbiter Surface Pressures with Flight Measurements," AIAA Paper 82-0937, June 1982.

[5]Weilmuenster, K. J. and Hamilton, H. H. II, "Calculations of Inviscid Flow over Shuttle-Like Vehicles at High Angles of Attack and Comparisons with Experimental Data," NASA TP-2103, May 1983.

[6]Weilmuenster, K. J., "High Angle-of-Attack Inviscid Flow Calculations over a Shuttle-Like Vehicle with Comparisons to Flight Data," NASA TP-2103, May 1983.

[7]Cooke, J. C., "An Axially Symmetric Analogue for General Three-Dimensional Boundary Layers," Reports and Memoranda No. 3200, British Aeronautical Research Council, 1961.

[8]Hamilton, H. H., DeJarnette, F. R., and Weilmuenster, K. J., "Application of Axisymmetric Analogue for Calculating Heating in Three-Dimensional Flows," AIAA Paper 85-245, Jan. 1985.

[9]Zoby, E. V., Moss, J. N., and Sutton, K., "Approximate Convective Heating Equations for Hypersonic Flows," *Journal of Spacecraft and Rockets*, Vol. 18, Jan. 1981, pp. 67–70.

[10]Kemp, N. H., Rose, P. H., and Detra, R. W., "Laminar Heat Transfer Around Blunt Bodies in Dissociated Air," *Journal of the Aerospace Sciences*, Vol. 26, No. 7, July 1959, pp. 421–430.

[11]Knox, E. C. and Best, J. T. Jr., "Pressure Test on the Viking Lander Capsule at Mach Number 10," AEDC-TR-72-185, Dec. 1972.

[12]Zoby, E. V. and Simmonds, A. L., "Engineering Flow-Field Method with Angle-of-Attack Applications," *Journal of Spacecraft and Rockets*, Vol. 22, July–Aug. 1985, pp. 398–404.